Materials Science & Engineering A 717 (2018) 78–84

Contents lists available at ScienceDirect

Materials Science & Engineering A

journal homepage: www.elsevier.com/locate/msea

High-concentration carbon assists plasticity-driven hydrogen embrittlement in a Fe-high Mn steel with a relatively high stacking fault energy

Ibrahim Burkay Tuğluca[a,b], Motomichi Koyama[a,*], Burak Bal[b], Demircan Canadinc[c], Eiji Akiyama[d], Kaneaki Tsuzaki[a,e]

[a] *Department of Mechanical Engineering, Kyushu University, Motooka 744, Nishi-ku, Fukuoka 819-0395, Japan*
[b] *Department of Mechanical Engineering, Abdullah Gül University, 38080 Kayseri, Turkey*
[c] *Department of Mechanical Engineering, Koç University, Sarıyer, Istanbul 34450, Turkey*
[d] *Institute for Materials Research, Tohoku University, Katahira 2-1-1, Aoba-ku, Sendai 980-8577 Japan*
[e] *HYDROGENIOUS, Kyushu University, Motooka 744, Nishi-ku, Fukuoka 819-0395, Japan*

ARTICLE INFO

Keywords:
Hydrogen embrittlement
High-manganese austenitic steel
Tension test
Stacking fault energy
Microstructure
Electron channelling contrast imaging

ABSTRACT

We investigated the effects of electrochemical hydrogen charging on the mechanical properties of a Fe-33Mn-1.1C austenitic steel with high carbon concentration and relatively high stacking fault energy. Hydrogen pre-charging increased the yield strength and degraded the elongation and work-hardening capability. The increase in yield strength is a result of the solution hardening of hydrogen. A reduction in the cross-sectional area by subcrack formation is the primary factor causing reduction in work-hardening ability. Fracture modes were detected to be both intergranular and transgranular regionally. Neither intergranular nor transgranular cracking modes are related to deformation twinning or simple decohesion in contrast to conventional Fe-Mn-C twinning-induced plasticity steels. The hydrogen-assisted crack initiation and subsequent propagation are attributed to plasticity-dominated mechanisms associated with strain localization. The occurrence of dynamic strain aging by the high carbon content and ease of cross slip owing to the high stacking fault energy can cause strain/damage localization, which assists hydrogen embrittlement associated with the hydrogen-enhanced localized plasticity mechanism.

1. Introduction

The stable austenitic phase has an advantage for hydrogen embrittlement resistance in terms of low hydrogen diffusivity [1,2], compared to BCC-based microstructures such as martensite and ferrite or metastable austenite. To control austenite stability, austenitic steels contain solute elements such as Ni [3], Cr [3], Mn [4], N [5], and C [6,7]. Since Cr, Ni, and N have been used as typical solute elements for austenitic stainless steels, their roles in electrochemical and mechanical properties [3,5,8] have been well investigated. Accordingly, hydrogen embrittlement resistance has also been examined with respect to equivalent Ni content [9,10]. By contrast, Mn has a negative role in corrosion resistance [11,12]; therefore, Mn has normally been avoided in stainless steels. However, demands for investigation into Mn effect on hydrogen embrittlement in austenitic steels have recently increased because of the occurrence of delayed fractures or hydrogen embrittlement of high-strength Mn steels such as twinning-induced plasticity (TWIP) steels [13,14]. In terms of "high-strength" Mn steel, the simultaneous addition of carbon is also crucial because the work-hardening capability is enhanced by Mn-C coupling [15,16], and even causes negative strain rate sensitivity of flow stress [17]. In fact, the presence of carbon also plays an important role in the hydrogen embrittlement resistance of high-Mn steels because carbon significantly influences various factors that affect hydrogen embrittlement resistance such as strain aging and martensitic transformation behaviors.

Specifically, factors affecting the hydrogen embrittlement resistance in high-Mn steels are twin density [18,19], martensitic transformability [20,21], strain aging hardenability [22,23], grain boundary character [13], and hydrogen uptake behavior [24–26]. In particular, the effects of twin and martensite become significant when the stacking fault energy (SFE) is low. Since Hadfield and TWIP steels with low SFE are practically important for automobiles, the effects of twin and HCP martensite on the behavior of hydrogen embrittlement has been elucidated. However, even without hydrogen, carbon can deteriorate the ductility when the SFE and carbon content are relatively high [27]. The negative carbon effect is associated with dynamic strain aging (DSA), which results in localized plasticity. The localized plasticity accelerates the occurrence of ductile fracture [27]. It is speculated that the carbon

---

[*] Corresponding author.
E-mail address: koyama@mech.kyushu-u.ac.jp (M. Koyama).

https://doi.org/10.1016/j.msea.2018.01.087
Received 10 January 2018; Received in revised form 19 January 2018; Accepted 22 January 2018

effect on plasticity might affect hydrogen embrittlement behavior associated with hydrogen-enhanced localized plasticity (HELP) [28] because of the similarity of their natures. In spite of the predicted carbon effect on the plasticity-driven hydrogen embrittlement of high-Mn steels, a detailed investigation of the carbon effect on this is lacking so far.

In this study, we focus on the hydrogen embrittlement behavior of a Fe-33Mn-1.1C steel that has been reported to show ductility degradation by DSA even without a hydrogen uptake [27]. By comparison with a result with hydrogen charging, we clarify the embrittlement behavior stemming from the effect of co-working carbon and hydrogen. Specifically, we found that the high-concentration solute carbon assists occurrence of plasticity-driven hydrogen embrittlement when stacking fault energy is relatively high compared with other Fe-Mn-C austenitic steels such as TWIP steels. In this paper, we therefore propose the new effects of a high carbon concentration and high SFE on the hydrogen embrittlement susceptibility of high-Mn steels.

2. Experimental procedure

An ingot of Fe-33Mn-1.1C steel (mass%) was prepared by a vacuum induction melting furnace. The ingot was forged and rolled at 1273 K. The rolled bar was solution-treated at 1273 K for 1 h, followed by water quenching. An average grain size was measured to be 33 μm. The detailed chemical composition is listed in Table 1. Tensile specimens were cut from the bar by electric discharge machining (EDM) to the gauge geometry with the dimensions of 4 mm in width, 1 mm in thickness, and 30 mm in length. The EDM layer was removed by chemical polishing with a H_2O_2:HF = 10:1 solution.

Tensile tests were carried out at 303 K at an initial strain rate of 10^{-2} s^{-1} with and without hydrogen precharging. The deformation temperature was controlled by a thermostatic chamber equipped with a tensile machine. Hydrogen was introduced by electrochemical charging before tensile tests at 353 K for 72 h in 3% (mass%) NaCl aqueous solution including 3 g/L NH_4SCN. The current density was fixed at 100 A/m^2 with a platinum wire counter electrode. In order to remove a thin contamination layer on the specimen surface by friction, the specimen was mechanically polished only with water on buff for 20 min every 12 h. After this water-polishing process, the thickness of the specimen did not change, but a shiny surface appeared. The diffusible hydrogen content was 44.0 mass ppm, which was measured by thermal desorption spectroscopy (TDS) from room temperature up to 660 K. The heating rate was 400 K/h. The diffusible hydrogen was defined as that corresponding to the first peak of the TDS profile, which appears in a temperature range from room temperature to 573 K. The first peak in high-Mn steels was reported to disappear after exposure to air at room temperature [24].

Microstructural characterization was carried out by using scanning electron microscopy. The fracture surface was observed by secondary electron (SE) imaging. Crystallographic feature and dislocation patterns were observed by electron backscatter diffraction (EBSD) measurement and electron channelling contrast imaging (ECCI), respectively. The specimen for EBSD and ECCI was prepared by mechanical polishing using colloidal silica with a particle size of 60 nm. The EBSD and ECCI were operated at acceleration voltages of 15 and 30 kV, respectively.

Table 1
Chemical composition of steel used (mass%).

C	Si	Mn	P	S	Cu	Fe
1.12	0.03	32.6	< 0.01	0.01	< 0.002	Bal.

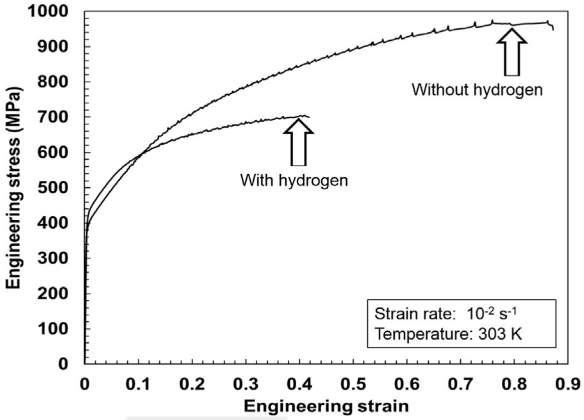

Fig. 1. Engineering stress-strain curves with and without hydrogen charging.

3. Results

3.1. Hydrogen effects on stress-strain response

Fig. 1 shows the engineering stress-strain (SS) curves of the specimens with and without hydrogen charging. The serrated flow on the SS curves results from DSA [15–17]. The total elongation was reduced by the hydrogen charging from 87% to 43%. Additionally, the hydrogen charging increased yield strength, and degraded the work-hardening capability. For the sake of clarification, work-hardening rates with and without hydrogen charging are plotted against the true strain in Fig. 2. In particular, the introduction of hydrogen reduced the work-hardening rate even at an early stage of deformation. In terms of fracture condition, as reported previously [27], the Fe-33Mn-1.1C steel without hydrogen pre-charging showed the failure before the plastic instability condition (Considère criterion) [29], which was caused by localized plasticity associated with DSA. On the other hand, the fracture of the Fe-33Mn-1.1C steel with hydrogen pre-charging occurred after satisfying Considère criterion, because of the drastic reduction in work hardening rates. Also note that the failure occurred immediately after satisfying the Considère criterion in the specimen with hydrogen pre-charging.

3.2. Characterization of the fracture surface and its vicinity

Fig. 3(a) shows the fracture surface of the specimen charged with hydrogen. The darker region near the specimen surface indicates a brittle-like fracture feature, and the central region is a completely ductile feature consisting of dimples. The brittle fracture zone depth is

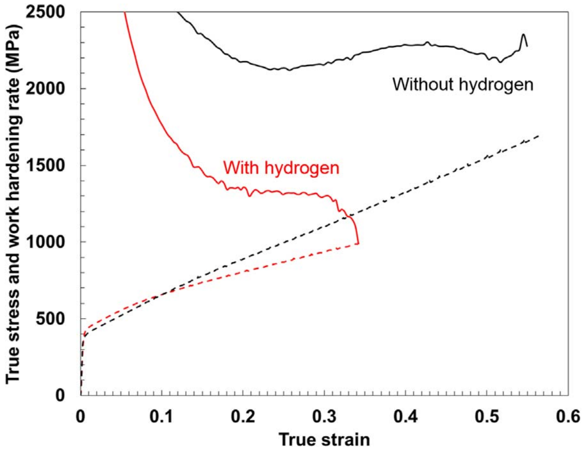

Fig. 2. Work hardening rates plotted against true strain corresponding to Fig. 1.

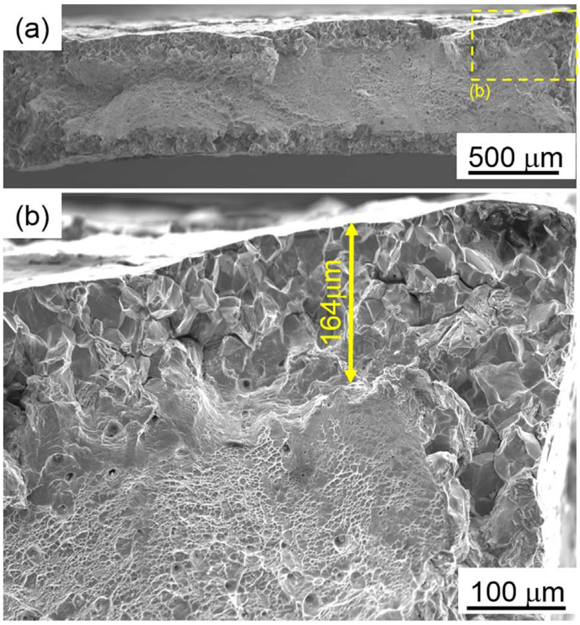

Fig. 3. (a) Overview of fracture surface of specimen with hydrogen charging. (b) Magnified image of region outlined in part (a).

estimated to be over 150 μm in depth. For example, the brittle fracture zone shown in Fig. 3(b) exhibits a 164-μm-hydrogen-affected zone. The area fraction of the brittle fracture zone on the fracture surface is 45%.

Fig. 4(a) shows details of the brittle fracture region with the effect of hydrogen. Intergranular features are dominant on the fracture surface; however, a quasi-cleavage feature was also observed, as indicated by yellow arrows. Even in the intergranular fracture region, slip traces were observed, as shown in Fig. 4(b), which is an indication of the contribution of plasticity to the intergranular cracking. Moreover, the microstructure underneath the fracture surface is shown in Fig. 5. The grains underneath the fracture surface shows a considerable amount of deformation twins that appear as dark contrast in the image quality map, while the grains in the second line from the fracture surface (below the white dotted line) show a distinctly smaller number of deformation twins, which indicates that a degree of the plastic deformation is significantly localized near the fracture edge in the grain-size-scale.

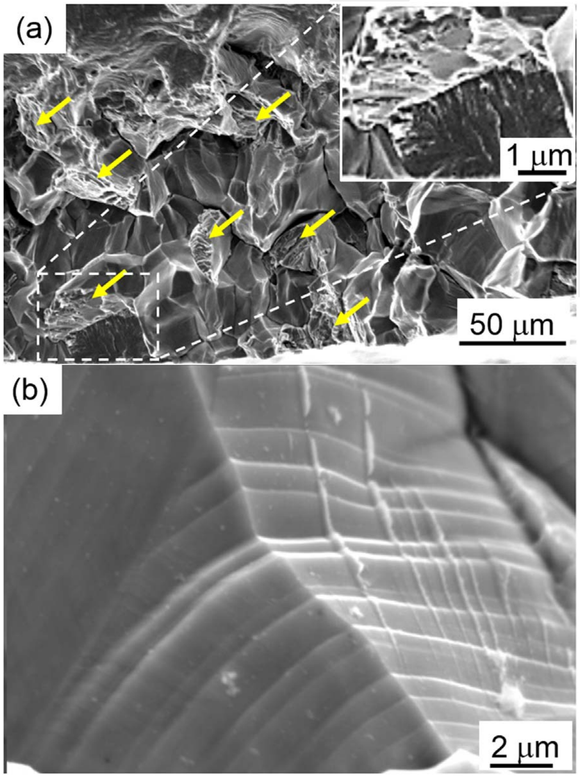

Fig. 4. (a) SE image of brittle-like fracture region. The inset indicates a magnified image showing quasi-cleavage feature. (b) Appearance of slip/twin traces on intergranular fracture region. (For interpretation of the references to color in this figure, the reader is referred to the web version of this article.)

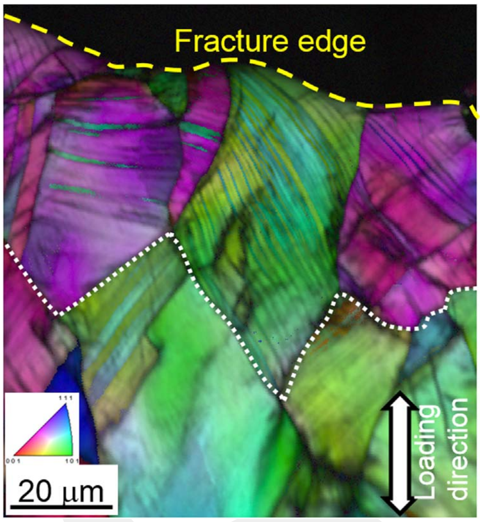

Fig. 5. Image quality map overlapped on an inverse pole figure map of loading direction near the fracture surface.

3.3. Microstructural characterization of subcracks

Fig. 6 shows a specimen surface after 5% strain with hydrogen precharging. Note that a considerable number of cracks appeared even at the early stage of deformation. The 5%-strain-induced cracks disappeared after 40 μm of mechanical polishing. Fig. 7 shows the specimen surface image after fracture with the hydrogen pre-charging. In contrast to the 5%-strain-induced cracks, numerous subcracks were observed in the fractured specimen even after 80 μm of mechanical polishing, which indicates that the crack depth increased with increasing strain.

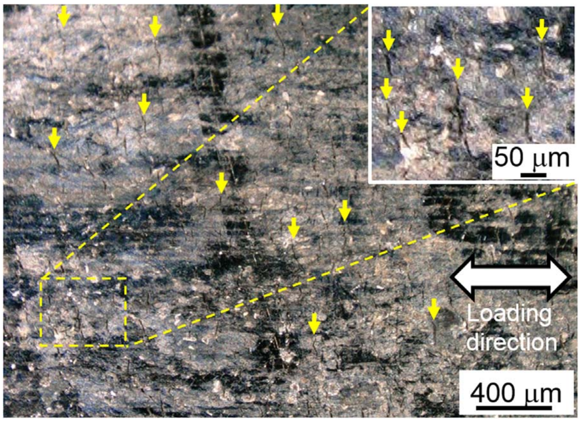

Fig. 6. Optical micrograph showing subcracks on the specimen surface after 5% deformation with hydrogen pre-charging. The yellow arrows indicate surface cracks. The inset indicates a magnified image of the region highlighted by the dashed square. (For interpretation of the references to color in this figure legend, the reader is referred to the web version of this article.)

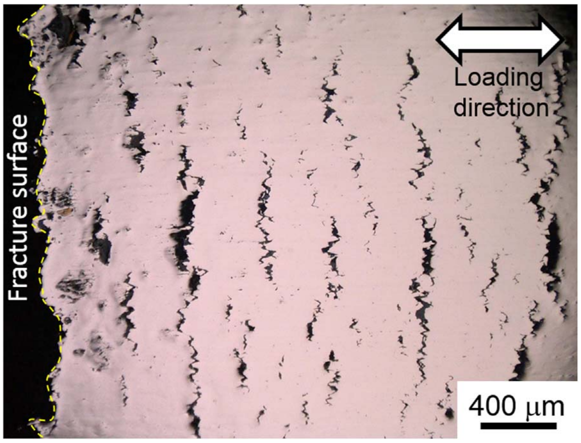

Fig. 7. Optical micrograph showing surface subcracks of the fractured specimen pre-charged with hydrogen.

Fig. 8 shows an ECC image that demonstrates a subcrack lying along a grain boundary. The deformation twin plates in the left grain are parallel to the subcrack. The right grain shows deformation twin plates perpendicular to the grain boundary, but the region where the subcrack exists does not show any deformation twin plates. Although a deformation twin bundle forms at a tip of the crack, the crack blunts, which indicates the formation of the deformation twin bundle did not contribute to the crack growth. As shown in an inset of Fig. 8(a), a high-dislocation density region exists between the twin plates, but no nanotwin was observed. Another crack initiation site was observed to be intersections of the twin plates, as shown in Fig. 8(b). The correlation between the crack and twin intersection is more clearly exhibited in Fig. 8(c). Furthermore, some cracks were observed between twins, as indicated by yellow arrows in Fig. 8(b). The cracks lie neither on the primary slip plane nor the twin plates.

Fig. 9 shows cracks that propagated slightly to a length less than the grain size. Assuming that the central position of the crack is a crack initiation site, most of the cracks presented in Fig. 9(a) formed from the grain boundary or twin-twin intersections, similarly to those in Fig. 8. These cracks propagated to the grain interior (central part of the image) or on the grain boundary (right part of the image). The transgranular crack growth path is in a region between twin plates, not on the deformation twin boundary. Similarly to Fig. 8(a), a high-dislocation-density region or cell walls formed between the twin plates, as shown in Fig. 8(b).

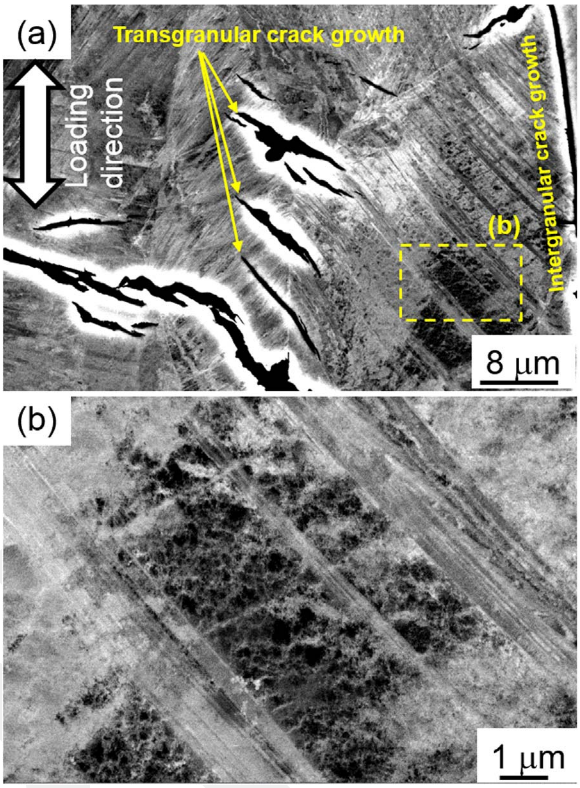

Fig. 9. (a) ECC image showing cracks that propagate into region between twin plates in the fractured specimen pre-charged with hydrogen. (b) Dislocation cell formation between twin plates.

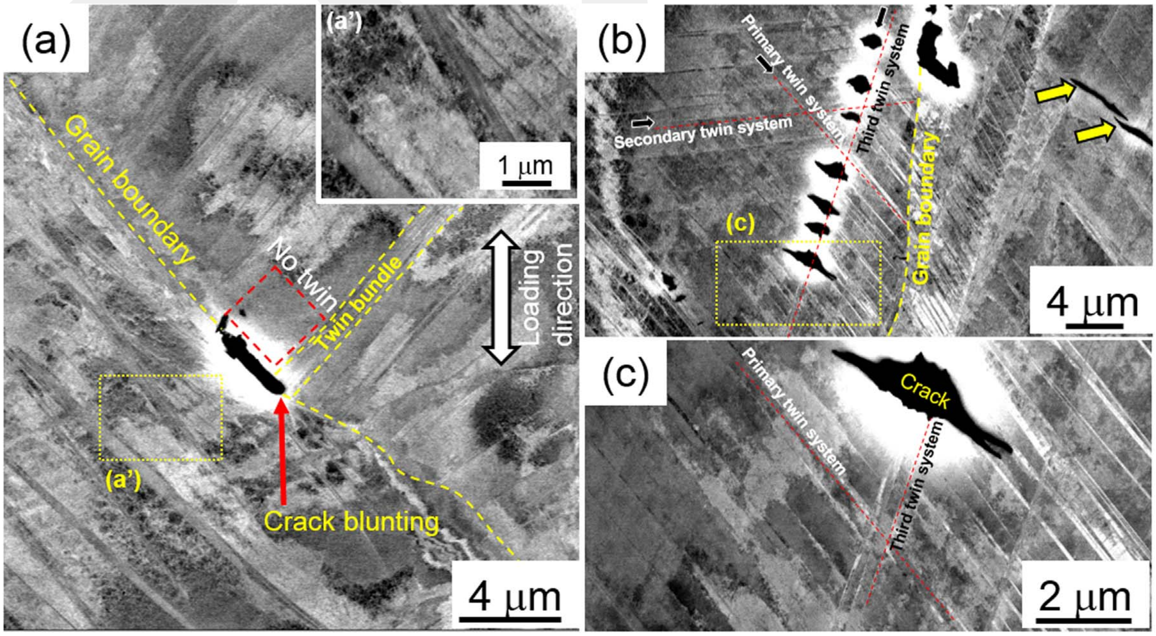

Fig. 8. (a) ECC image showing a subcrack of the fractured specimen pre-charged with hydrogen. Yellow broken line indicates a grain boundary. Inset (a′) shows magnified image of region outlined in part (a). (b) Crack initiation at intersections of deformation twins. (c) Magnified image of region outlined in part (b). (For interpretation of the references to color in this figure legend, the reader is referred to the web version of this article.)

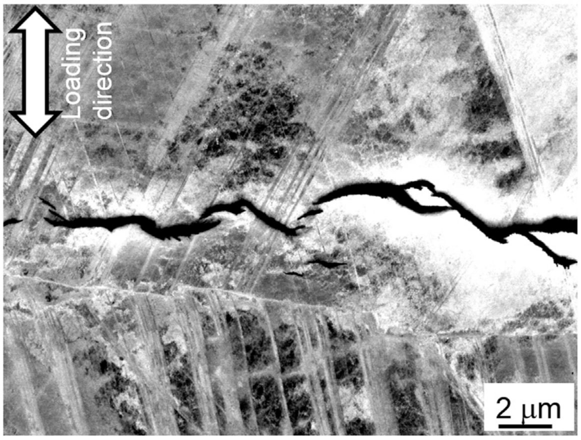

Fig. 10. ECC image showing curved-crack cross deformation twin plates in the fractured specimen pre-charged with hydrogen.

The important characteristic of the transgranular crack growth is that the propagation path is not along the twin and slip planes. Fig. 10 shows clear evidence of crack growth without crystallographic features. The crack shown in Fig. 10 demonstrates a curved shape and propagates across the primary and secondary twin plates. Therefore, the crack growth mode cannot be directly correlated to any crystallographic feature such as the twin boundary or slip plane.

4. Discussion

According to microstructure and fracture surface observations, the characteristic hydrogen effects in the high-Mn steel with a relatively high SFE and high carbon content are as follows:

(1) The hydrogen uptake increased the yield strength and decreased the work-hardening rate, which caused the deterioration of elongation.
(2) The crack initiation sites are the grain boundary, twin-twin intersections, and part of the grain interior.
(3) The macroscopic hydrogen-assisted failure is associated with a plasticity-based mechanism, which might be associated with HELP.
(4) Intergranular cracking is associated with plastic deformation: clear slip/twin traces are observed on the fracture surface.
(5) The transgranular crack propagation path does not have specific crystallographic features.

Therefore, we mainly discuss how the work-hardening rate was decreased by the hydrogen uptake. The degradation mechanism must be correlated with the dislocation pattern, crack initiation, and its propagation.

4.1. Mechanisms of the enhanced yield strength and reduced work-hardening capability and ductility

Hydrogen-degraded elongation and strength in Fe-high-Mn austenitic steels have been observed in previous studies [2,13]; however, degradation of the work-hardening rate by hydrogen uptake is not a common phenomenon in the steel series. In this section, we discuss the macroscopic effect of hydrogen on mechanical properties, i.e., the increased yield strength and decreased work-hardening rate.

The increased yield strength in austenitic steels has been reported to arise from the solution hardening of hydrogen. For instance, Abraham et al. reported an approximately 50-MPa increase in the yield strength at 295 K in a type-301s austenitic stainless steel with a hydrogen content of 1 at% [30]. On the one hand, the hydrogen uptake in the present steel provided a negative effect on work-hardening rates. The metallurgical main factors affecting the work-hardening rate in the present steel are dynamic strain aging and deformation twinning. In addition, as seen in Figs. 6 and 7, a considerable number of cracks were induced by the hydrogen effect. The cracks formed even at an early deformation stage such as 5% strain (Fig. 6). Therefore, a reduction in the cross-sectional area stemming from the crack formation is another factor in reducing the apparent work-hardening rate.

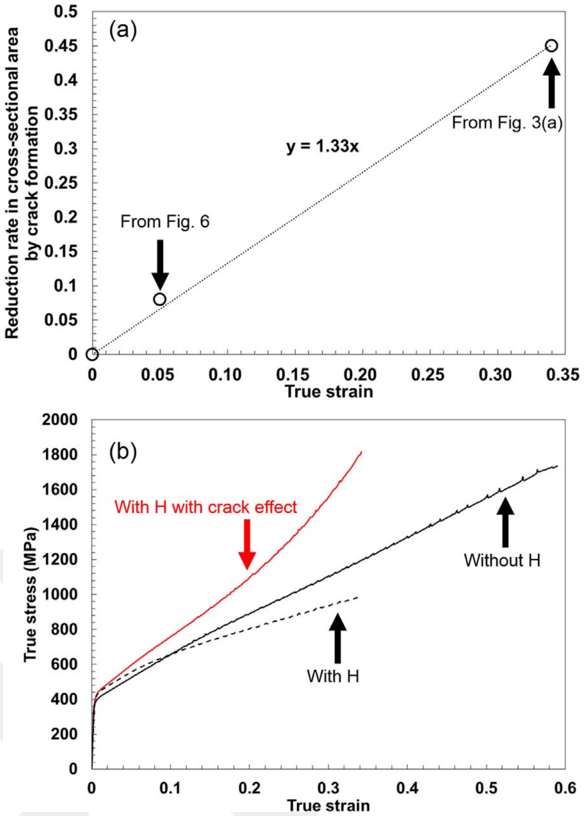

Fig. 11. (a) Relationship between true strain and reduction rate in cross-sectional area by crack formation. (b) Estimated true stress-strain curve (red curve) containing the effect of crack formation calculated based on (a) and Eq. (2). (For interpretation of the references to color in this figure legend, the reader is referred to the web version of this article.)

Assuming a half-penny-shaped crack, the average area of a surface crack at 5% strain is estimated to be 5500 μm^2. The number of surface cracks at 5% strain was approximately six per 1 mm along the direction perpendicular to the loading axis. Since the width and thickness of the specimen were 4 and 1 mm, respectively, 60 surface cracks with the total crack area of 0.33 mm^2 can lie on an identical cross-sectional plane of the specimen. That is, the crack formation can reduce the cross-sectional area from 4.0 mm^2 to 3.7 mm^2 at 5% strain. Accordingly, an 8% reduction in the 5% flow stress is caused by the crack formation. In addition, assuming that the ductile fracture zone shown in Fig. 3(a) corresponds to the remaining cross-sectional area immediately before satisfying the Considère criterion, the true stress at 0.34 true strain is reduced by 49% by the crack formation. The effect of crack formation on the cross-sectional area is shown in Fig. 11(a). The reduction rate in the cross-sectional area by the crack formation was defined as

$$\delta_{Ac} = A_c/A_0 \tag{1}$$

where A_0 and A_c are the total cross-sectional area and brittle-like crack area at an arbitrary strain, respectively. With the linearly approximated relationship between the true strain and reduction in the cross-sectional area, the true stress containing the effect of crack formation in the hydrogen-charged specimen can be obtained by

$$\sigma_{t/withc} = \sigma_t \bullet (1 - 1.33\varepsilon_t)^{-1} \tag{2}$$

where σ_t and ε_t are the true stress and true strain, respectively. The true stress-strain curve estimated by Eq. (2) is shown in Fig. 11(b). The effect of crack formation explains the reduction in the flow stress and work-hardening rate. The calculated true stress is even larger than that without hydrogen charging, which is attributed to an effect of stress triaxiality arising from the presence of a crack, i.e., notch strengthening [31].

4.2. Crack initiation mechanisms

Three types of crack initiation sites were observed in the hydrogen-precharged steel. The first and second types of crack initiation sites are the grain boundary and twin-twin intersection, which are the same as in previous reports [2,19,32,33]. The crack initiation at the twin-twin intersection can be interpreted by microstress concentration [18,19,34,35]. In high-Mn steels with a low SFE such as TWIP steel, intergranular cracking can be induced by the formation of a deformation twin that is impinged at the grain boundaries [19]. However, as observed in Fig. 8(a), intergranular cracking is not attributed to the impingement of deformation twin growth. Instead, high dislocation density and cell walls were observed near the grain boundary where cracking occurs. These observation results indicate that the intergranular crack formation arises from slip localization perhaps associated with HELP [36,37]. Correspondingly, slip traces were observed in the intergranular fracture region, as shown in Fig. 4(b), which supports the occurrence of plasticity-assisted intergranular cracking in the hydrogen-charged steel. Here, note that the hydrogen increased yield strength, that is, solution "hardening" occurred. This fact indicates that the HELP effect does not stem from a softening effect of hydrogen on single dislocation mobility. The hydrogen would contribute to localized plasticity associated with interactions of multiple dislocations, e.g. suppression of long range stress fields by reducing repulsive interaction between dislocations [38].

The third type of crack initiation sites is a significant finding: the crack was initiated within a grain interior that is not associated with twins, as observed in Fig. 8(b). Since there is no specific crystallographic feature in the transgranular cracks, a possible crack initiation site is the cell wall observed in Figs. 8(a′) and 9(b). In fact, the cell wall has been recognized as a preferential hydrogen-assisted damage initiation site in steels [39]. Since cell wall is an aggregate of lattice defects, microdamage initiation, coalescence, and growth may preferentially occur in the cell walls. In the present steel, the occurrence of DSA assists plastic strain localization, and the high SFE enables cross slip easily. The special characteristics cause hydrogen-related damage localization, which can induce cell-wall cracking and plasticity-assisted intergranular cracking.

4.3. Crack propagation mechanism

According to the fracture surface observations (Figs. 3 and 4), the hydrogen-assisted crack propagation occurred via quasi-cleavage and intergranular cracking. In terms of intergranular cracking, the crack growth is discontinuous because crack blunting was observed in Fig. 8(a). Furthermore, the slip trace in the intergranular fracture region, e.g., in Fig. 4(b), was generally observed on the fracture surface, which indicates the occurrence of plastic deformation during crack growth. In other words, the hydrogen-assisted intergranular crack propagation progresses via the repetition of crack blunting, plastic damage/diffusible hydrogen accumulations at a crack tip, and subsequent crack growth.

From the viewpoint of transgranular cracking, the crack growth path did not show crystallographic features, as observed in Figs. 9 and 10, unlike Fe-Mn-C TWIP steels where crack growth was observed along the primary and secondary deformation twins [19]. In the same context as the transgranular crack initiation mechanism, the curved crack propagation path can be interpreted by a plasticity-based mechanism, that is, the dislocation accumulation that forms cell walls can cause the transgranular crack propagation. Consequently, both the intergranular and transgranular crack propagation are mainly attributed to plasticity-based mechanisms, which are not related to deformation twinning or simple decohesion. As mentioned in the introduction, the present steel with high SFE and carbon content causes plasticity-induced premature fractures even without hydrogen, which is associated with the occurrence of DSA [27]. The combined effect of HELP and DSA-assisted plasticity localization causes the remarkable degradation of elongation and strength, which is different hydrogen embrittlement behavior from low-SFE high-Mn steels where martensitic transformation or deformation twinning occurs. Accordingly, the plastic deformation degree near intergranular or transgranular fracture surface was entirely higher than that in a region slightly far from the fracture edge as shown in Fig. 5.

Consequently, we presented that the high carbon concentration assists plasticity-driven hydrogen embrittlement in the Fe-Mn-C austenitic steel with the high SFE. Note that we do not exclude other factors that trigger hydrogen embrittlement, e.g., vacancy accumulation [40,41] and reduction in cohesive energy [42]. As we claimed previously for a precipitation-strengthened austenitic steel [43], the microplasticity evolution causes hydrogen and vacancy localization, which may assist occurrence of decohesion or vacancy-induced failure.

5. Conclusions

The hydrogen embrittlement behavior of a Fe-33Mn-1.1C steel was investigated in this study. Characteristics of the steel used are (1) high stacking fault energy and (2) high carbon concentration. Electrochemical hydrogen charging resulted in an increase in yield strength. Contrary to improvements in yield strength, the work-hardening rate and elongation were affected negatively by hydrogen uptake. Conclusions of this study are as follows:

1. Yield strength of the Fe-Mn-C steel increased owing to the solution hardening of hydrogen.
2. Subcrack formation is the major reason for decreases in the apparent work-hardening rate, which accordingly results in reduced elongation.
3. Intergranular cracks were initiated owing to slip localization stemming from a HELP mechanism, and subsequently propagated via crack blunting and strain localization.
4. Quasi-cleavage cracking was caused by DSA and HELP-driven plastic strain localization, not by twin boundary cracking. The high stacking fault energy of the steel would assist the strain localization because of ease of cross slip. Furthermore, transgranular crack propagation results from dislocation accumulation that formed cell walls.

Acknowledgements

This work was financially supported by JSPS KAKENHI (JP16H06365 and JP17H04956) and the Japan Science and Technology Agency (JST) (Grant number: 20100113) under Industry-Academia Collaborative R&D Program "Heterogeneous Structure Control: Towards Innovative Development of Metallic Structural Materials."

References

[1] C. San Marchi, B.P. Somerday, X. Tang, G.H. Schiroky, Effects of alloy composition and strain hardening on tensile fracture of hydrogen-precharged type 316 stainless steels, Int. J. Hydrog. Energy 33 (2) (2008) 889–904.
[2] M. Koyama, E. Akiyama, Y.-K. Lee, D. Raabe, K. Tsuzaki, Overview of hydrogen embrittlement in high-Mn steels, Int. J. Hydrog. Energy 42 (17) (2017) 12706–12723.
[3] K.H. Lo, C.H. Shek, J.K.L. Lai, Recent developments in stainless steels: R: reports, Mater. Sci. Eng. 65 (4) (2009) 39–104.
[4] Y. Tomota, M. Strum, J.W. Morris, Microstructural dependence of Fe-high Mn tensile behavior, Metall. Trans. A 17 (3) (1986) 537–547.

[5] J.W. Simmons, Overview: high-nitrogen alloying of stainless steels, Mater. Sci. Eng.: A 207 (2) (1996) 159–169.

[6] T. Ogawa, M. Koyama, C.C. Tasan, K. Tsuzaki, H. Noguchi, Effects of martensitic transformability and dynamic strain age hardenability on plasticity in metastable austenitic steels containing carbon, J. Mater. Sci. 52 (13) (2017) 7868–7882.

[7] M. Koyama, T. Ogawa, D. Yan, Y. Matsumoto, C.C. Tasan, K. Takai, K. Tsuzaki, Hydrogen desorption and cracking associated with martensitic transformation in Fe-Cr-Ni-Based austenitic steels with different carbon contents, Int. J. Hydrog. Energy 42 (42) (2017) 26423–26435.

[8] D.M. Symons, Hydrogen embrittlement of Ni-Cr-Fe alloys, Metall. Mater. Trans. 28 (3) (1997) 655–663.

[9] L. Zhang, M. Wen, M. Imade, S. Fukuyama, K. Yokogawa, Effect of nickel equivalent on hydrogen gas embrittlement of austenitic stainless steels based on type 316 at low temperatures, Acta Mater. 56 (14) (2008) 3414–3421.

[10] O.A. El kebir, A. Szummer, Comparison of hydrogen embrittlement of stainless steels and nickel-base alloys, Int. J. Hydrog. Energy 27 (7) (2002) 793–800.

[11] Y.H. Jang, S.S. Kim, J.H. Lee, Effect of different Mn contents on tensile and corrosion behavior of CD4MCU cast duplex stainless steels, Mater. Sci. Eng.: A 396 (1) (2005) 302–310.

[12] A. Chiba, I. Muto, Y. Sugawara, N. Hara, Pit initiation mechanism at MnS inclusions in stainless steel: synergistic effect of elemental sulfur and chloride ions, J. Electrochem. Soc. 160 (10) (2013) C511–C520.

[13] Y.S. Chun, K.-T. Park, C.S. Lee, Delayed static failure of twinning-induced plasticity steels, Scr. Mater. 66 (12) (2012) 960–965.

[14] M. Koyama, E. Akiyama, K. Tsuzaki, Hydrogen embrittlement in a Fe–Mn–C ternary twinning-induced plasticity steel, Corros. Sci. 54 (2012) 1–4.

[15] Y. Dastur, W. Leslie, Mechanism of work hardening in Hadfield manganese steel, Metall. Trans. A 12 (5) (1981) 749–759.

[16] S.-J. Lee, J. Kim, S.N. Kane, B.C.D. Cooman, On the origin of dynamic strain aging in twinning-induced plasticity steels, Acta Mater. 59 (17) (2011) 6809–6819.

[17] D. Canadinc, C. Efstathiou, H. Sehitoglu, On the negative strain rate sensitivity of Hadfield steel, Scr. Mater. 59 (10) (2008) 1103–1106.

[18] M. Koyama, E. Akiyama, T. Sawaguchi, D. Raabe, K. Tsuzaki, Hydrogen-induced cracking at grain and twin boundaries in an Fe–Mn–C austenitic steel, Scr. Mater. 66 (7) (2012) 459–462.

[19] M. Koyama, E. Akiyama, K. Tsuzaki, D. Raabe, Hydrogen-assisted failure in a twinning-induced plasticity steel studied under in situ hydrogen charging by electron channeling contrast imaging, Acta Mater. 61 (12) (2013) 4607–4618.

[20] Y.S. Chun, J.S. Kim, K.-T. Park, Y.-K. Lee, C.S. Lee, Role of ε martensite in tensile properties and hydrogen degradation of high-Mn steels, Mater. Sci. Eng.: A 533 (2012) 87–95.

[21] M. Koyama, S. Okazaki, T. Sawaguchi, K. Tsuzaki, Hydrogen embrittlement susceptibility of Fe-Mn binary alloys with high Mn content: effects of stable and metastable ε-martensite, and Mn concentration, Metall. Mater. Trans. A 47 (2016) 2656–2673.

[22] M. Koyama, E. Akiyama, K. Tsuzaki, Hydrogen-induced delayed fracture of a Fe–22Mn–0.6C steel pre-strained at different strain rates, Scr. Mater. 66 (11) (2012) 947–950.

[23] M. Koyama, E. Akiyama, K. Tsuzaki, Effects of static and dynamic strain aging on hydrogen embrittlement in TWIP steels containing Al, ISIJ Int. 53 (7) (2013) 1268–1274.

[24] M. Koyama, E. Akiyama, K. Tsuzaki, Effect of hydrogen content on the embrittlement in a Fe–Mn–C twinning-induced plasticity steel, Corros. Sci. 59 (2012) 277–281.

[25] I.-J. Park, K.-H. Jeong, J.-G. Jung, C.S. Lee, Y.-K. Lee, The mechanism of enhanced resistance to the hydrogen delayed fracture in Al-added Fe–18Mn–0.6C twinning-induced plasticity steels, Int. J. Hydrog. Energy 37 (12) (2012) 9925–9932.

[26] H.-H. Jeon, S.-M. Lee, J. Han, I.-J. Park, Y.-K. Lee, The effect of Zn coating layers on the hydrogen embrittlement of hot-dip galvanized twinning-induced plasticity steel, Corros. Sci. 111 (2016) 267–274.

[27] M. Koyama, Y. Shimomura, A. Chiba, E. Akiyama, K. Tsuzaki, Room-temperature blue brittleness of Fe-Mn-C austenitic steels, Scr. Mater. 141 (2017) 20–23.

[28] I.M. Robertson, P. Sofronis, A. Nagao, M.L. Martin, S. Wang, D.W. Gross, K.E. Nygren, Hydrogen embrittlement understood, Metall. Mater. Trans. B 46 (3) (2015) 1085–1103.

[29] M. Koyama, T. Sawaguchi, K. Tsuzaki, TWIP effect and plastic instability condition in an Fe–Mn–C austenitic steel, ISIJ Int. 53 (2) (2013) 323–329.

[30] D.P. Abraham, C.J. Altstetter, The effect of hydrogen on the yield and flow stress of an austenitic stainless steel, Metall. Mater. Trans. A 26 (11) (1995) 2849–2858.

[31] R. Abbaschian, R.E. Reed-Hill, Physical Metallurgy Principles, Cengage Learning, Stamfrord, CT, 2008.

[32] J.H. Ryu, S.K. Kim, C.S. Lee, D.-W. Suh, H.K.D.H. Bhadeshia, Effect of aluminium on hydrogen-induced fracture behaviour in austenitic Fe–Mn–C steel, Proc. R. Soc. A: Math. Phys. Engi. Sci. 469 (2149) (2013).

[33] B. Bal, M. Koyama, G. Gerstein, H.J. Maier, K. Tsuzaki, Effect of strain rate on hydrogen embrittlement susceptibility of twinning-induced plasticity steel pre-charged with high-pressure hydrogen gas, Int. J. Hydrog. Energy 41 (34) (2016) 15362–15372.

[34] P. Müllner, C. Solenthaler, P.J. Uggowitzer, M.O. Speidel, Brittle fracture in austenitic steel, Acta Metall. Mater. 42 (7) (1994) 2211–2217.

[35] P. Müllner, On the ductile to brittle transition in austenitic steel, Mater. Sci. Eng.: A 234 (1997) 94–97.

[36] M.L. Martin, B.P. Somerday, R.O. Ritchie, P. Sofronis, I.M. Robertson, Hydrogen-induced intergranular failure in nickel revisited, Acta Mater. 60 (6) (2012) 2739–2745.

[37] S. Wang, M.L. Martin, P. Sofronis, S. Ohnuki, N. Hashimoto, I.M. Robertson, Hydrogen-induced intergranular failure of iron, Acta Mater. 69 (Supplement C) (2014) 275–282.

[38] P.J. Ferreira, I.M. Robertson, H.K. Birnbaum, Hydrogen effects on the interaction between dislocations, Acta Mater. 46 (5) (1998) 1749–1757.

[39] M. Nagumo, Function of hydrogen in embrittlement of high-strength steels, ISIJ Int. 41 (6) (2001) 590–598.

[40] M. Nagumo, Hydrogen related failure of steels – a new aspect, Mater. Sci. Technol. 20 (8) (2004) 940–950.

[41] M. Hatano, M. Fujinami, K. Arai, H. Fujii, M. Nagumo, Hydrogen embrittlement of austenitic stainless steels revealed by deformation microstructures and strain-induced creation of vacancies, Acta Mater. 67 (2014) 342–353.

[42] M. Yamaguchi, K.-I. Ebihara, M. Itakura, T. Kadoyoshi, T. Suzudo, H. Kaburaki, First-principles study on the grain boundary embrittlement of metals by solute segregation: Part II. metal (Fe, Al, Cu)-hydrogen (H) systems, Metall. Mater. Trans. A 42 (2) (2011) 330–339.

[43] M. Koyama, H. Springer, S.V. Merzlikin, K. Tsuzaki, E. Akiyama, D. Raabe, Hydrogen embrittlement associated with strain localization in a precipitation-hardened Fe–Mn–Al–C light weight austenitic steel, Int. J. Hydrog. Energy 39 (9) (2014) 4634–4646.